robotics

MDPI

Article

Numerical and Experimental Validation of an Autonomous Navigation and Mapping Framework for Mobile Robotics †

Antonin Aufrere [1], Lorenzo Scalera [2,*], Eleonora Maset [2] and Alessandro Gasparetto [2]

1 Polytech Dijon, Université Bourgogne Europe, 21078 Dijon, France; aufrere.antonin03@gmail.com
2 Polytechnic Department of Engineering and Architecture, University of Udine, 33100 Udine, Italy; eleonora.maset@uniud.it (E.M.); alessandro.gasparetto@uniud.it (A.G.)
* Correspondence: lorenzo.scalera@uniud.it

† This paper is an extended version of our paper published in Tiozzo Fasiolo, D.; Scalera, L.; Maset, E.; Lesquerré-Caudebez, B.; Fusiello, A.; Beinat, A.; Gasparetto, A. A Navigation Approach for Autonomous Mobile Robots in Sustainable Agriculture. In *Proceedings of I4SDG Workshop 2025—IFToMM for Sustainable Development Goals. I4SDG 2025*; Carbone, G., Quaglia, G., Eds.; Mechanisms and Machine Science; Springer, Cham, Switzerland, 2025; Volume 179. https://doi.org/10.1007/978-3-031-91151-4_44.

Abstract

Autonomous navigation in agricultural environments remains a key challenge for the deployment of mobile robots in precision viticulture. In this paper, we present the numerical and experimental validation of a LiDAR–inertial navigation and mapping framework for mobile robots operating in vineyard-like scenarios. A realistic vineyard simulation environment reproducing the geometric structure of vine rows is first developed to evaluate the performance of the proposed framework, considering multiple metrics including mapping time, speed stability, path tracking error, and point cloud reconstruction density. Then, the proposed approach is tested in a real vineyard using a Scout 2.0 mobile robot. Numerical and experimental results demonstrate the feasibility of the navigation and mapping strategy and its robustness during extensive repeated tests in the field.

Keywords: autonomous navigation; 3D mapping; mobile robotics; path planning; vineyard

1. Introduction

Nowadays, autonomous mobile robots are increasingly in demand in agriculture for monitoring crops and gathering information on the health and quality of the plants [1]. Their development is closely aligned with several Sustainable Development Goals (SDGs) defined by the United Nations in the 2030 Agenda, including SDG 2 (Zero Hunger), SDG 6 (Clean Water and Sanitation), SDG 12 (Responsible Consumption and Production), and SDG 15 (Life on Land) [2]. By mapping and monitoring agricultural environments, mobile robots can collect valuable data to optimize resource usage, such as enabling variable-rate application of water and pesticides, and to enhance productivity through tasks like automated harvesting [3,4]. Moreover, the data acquired by these systems support environmentally responsible farm management, fostering ecosystem preservation and biodiversity conservation [5]. For example, 3D point clouds collected in vineyards can provide detailed information about plant height and volume, which can be used to evaluate the effects of different irrigation strategies [6,7]. In this way, 3D mapping technologies can contribute to improving crop health and increasing yields [8].

To operate effectively in unstructured agricultural settings, mobile robots must be capable of autonomous navigation, ensuring consistent and reliable monitoring of crops [9].

Academic Editor: Giovanni Muscato

Received: 19 May 2026
Revised: 11 June 2026
Accepted: 15 June 2026
Published: 16 June 2026

A key challenge in this context is path planning, which must account for both static and dynamic obstacles such as branches, leaves, trunks, and human workers [10–12]. Furthermore, autonomous navigation in vineyard also requires global and local path planning algorithms capable of steering the robot through vineyard rows [13,14], as well as to turning at the head of the rows [15,16]. Autonomous path planning can significantly reduce the need for manual operation; however, agricultural environments introduce several difficulties, including seasonal variability, that require tailored navigation strategies.

For instance, Santos et al. proposed a path planning approach specifically designed for steep-slope vineyards [17], while Schonegg et al. introduced a method based on 3D vineyard point clouds for autonomous navigation [18]. Additionally, Cerrato et al. developed a data-driven navigation approach based on occupancy grid representations of the field [19]. A comprehensive review of the state-of-the-art path planning and tracking control strategies for mobile robots in orchards can be found in [20].

Another major challenge is robot localization, i.e., estimating the full 6-degree-of-freedom (DOF) pose required to follow planned trajectories. Many systems rely on Global Navigation Satellite Systems (GNSS) enhanced with Real-Time Kinematics (RTK) and integrated with Inertial Measurement Units (IMUs) [21,22]. However, GNSS-based solutions may be unreliable in agricultural environments due to signal occlusion and multi-path effects [23]. As a result, alternative approaches such as Visual Odometry (VO), which leverages image data from onboard cameras, have been explored [24]. Nevertheless, repetitive visual patterns in row-crop environments can degrade performance. To address these limitations, Simultaneous Localization and Mapping (SLAM) techniques based on Light Detection and Ranging (LiDAR) data have been proposed to improve robustness [25,26]. For instance, in [27] an adaptive LiDAR odometry and mapping framework tailored for autonomous agricultural mobile robots operating in complex agricultural environments is presented. Furthermore, a global self-localization and navigation approach using 3D-LiDAR for headland turning in vineyards is proposed in [15].

Despite these advances, relatively few systems effectively integrate multiple sensing modalities into a robust SLAM framework capable of long-term operation and precise path repetition in complex vineyard scenarios. Alternatively, position-agnostic control strategies, which directly map sensor inputs to velocity commands without relying on a global reference frame, have been investigated for navigation between vineyard rows. For example, Aghi et al. proposed an approach based on image segmentation to identify a target point in the camera frame, which is then used to guide the robot [28].

In this context, virtual environments and datasets play a fundamental role in the development and validation of autonomous navigation systems for agricultural robots. Simulation platforms enable the testing of navigation algorithms under diverse and controlled conditions, such as varying terrain, crop arrangements, and environmental factors, without the risks and costs associated with real-world experiments [23,29,30]. At the same time, high-quality datasets provide realistic sensory inputs, including images, LiDAR scans, and positioning data, which are essential for training and benchmarking perception and localization algorithms [31–36]. The combined use of virtual environments and real-world datasets supports rapid prototyping, reproducibility, and robust performance evaluation, ultimately accelerating the deployment of reliable autonomous systems in agriculture.

In this paper, we present the numerical and experimental validation of a LiDAR–inertial navigation and mapping framework for mobile robots operating in vineyard-like environments. To evaluate the performance of the framework, we first develop a realistic vineyard simulation environment in Gazebo that reproduces the spatial structure of vine rows and integrates additional environmental landmarks to improve LiDAR observability. A series of controlled tests is then conducted at different robot speeds in order to evaluate navigation performance using several complementary metrics, including mapping duration, speed stability, path tracking error, and point cloud reconstruction density. The results obtained in simulation are then compared with extensive experiments performed in a real vineyard using a Scout 2.0 mobile robot. This combined analysis allows us to identify an optimal operating speed range for vineyard navigation and 3D mapping, as well as to verify that the speed-dependent trends observed in simulation hold under real-world conditions.

This work is an extended version of our previous study in [37]. With respect to [37], in this paper the following extensions are presented: (i) the development of a realistic virtual vineyard environment to test the navigation and mapping framework in controlled and repeatable conditions; (ii) an analysis of the influence of robot speed on trajectory tracking error, velocity stability, mapping duration, and point cloud reconstruction density; (iii) the results of extensive experimental tests in a real vineyard to demonstrate the robustness of the proposed framework and the repeatability of the autonomous navigation and mapping capabilities of the robot, also in terms of 3D reconstruction of the environment. Please note that the primary objective of this work is to assess the feasibility and repeatability of our proposed LiDAR–inertial navigation and mapping framework operating without GNSS in vineyard, and to compare its behavior in simulation and real-world conditions.

The remainder of the paper is structured as follows: Section 2 presents the proposed autonomous navigation and mapping framework. The numerical and experimental setup is described in Section 3. Section 4 illustrates and discusses the numerical and experimental results. Finally, Section 5 concludes the work and provides future developments.

2. Autonomous Navigation and Mapping Framework

The navigation strategy proposed in this work enables a mobile robot to autonomously operate in agricultural environments, particularly along vineyard rows for monitoring and mapping applications. The navigation framework relies on data from a LiDAR sensor, an IMU, and wheel odometry for localization and obstacle avoidance. A graphical overview of the proposed autonomous navigation and mapping framework is reported in Figure 1. In this work, we consider the mobile robot operating in vineyard-like environments without relying on GNSS measurements. This decision is made in order to compare the performance of the proposed navigation and mapping framework in the simulation environment, where GNSS cannot be implemented, and in the actual vineyard. Furthermore, while GNSS, particularly RTK-based solutions, are widely used for agricultural navigation, their reliability can be limited by vegetation coverage, signal occlusions, or multipath effects.

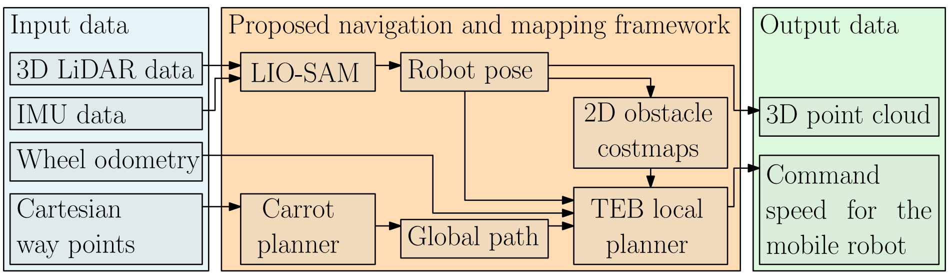

Figure 1. Overview of the proposed autonomous navigation and mapping framework.

The navigation approach guides the robot back and forth along each row of the vineyard before transitioning to the next one. The autonomous navigation system is indeed tailored for a mobile robot equipped with a side-mounted multispectral camera oriented toward the crop rows. With this setup, the sensor is limited to observing only one side of the vineyard corridor at a time, for instance, the right-hand side when the camera is installed on the robot right. Consequently, to achieve full coverage of both sides of each row, the robot traverses the corridor in alternating directions, performing back-and-forth passes along the vineyard rows. However, in this work we focus on the autonomous navigation of the robot and its 3D mapping capabilities, and no multispectral data is considered.

Assuming that vineyard corridors are free of static obstacles, the global path is defined by straight-line segments connecting consecutive way points. The Carrot Planner is used in this work as global path planner [38]. The Carrot Planner receives a goal point, adjusts it if it lies within an obstacle by moving it backward along the robot–goal direction until it becomes feasible, and then provides it to the local planner. It generates a path by connecting consecutive way points with straight segments, allowing the robot to approach each target as closely as possible.

However, this path may still expose the robot to potential collisions with branches, foliage, human operators, or other unexpected obstacles. To address this, the Timed Elastic Band (TEB) local path planner is used to perform real-time obstacle avoidance [39]. This collision avoidance system relies on online-generated 2D maps, constructed from the most recent LiDAR scans acquired by the mobile robot, to estimate the traversability risk of the surrounding environment. An example of the cost maps built online by proposed framework during navigation in the vineyard is shown in Figure 2. The visualizations in the figure are captured during navigation in the RViz software, ROS (Robot Operating System) Melodic, where the mobile robot is visible within the accumulated point cloud.

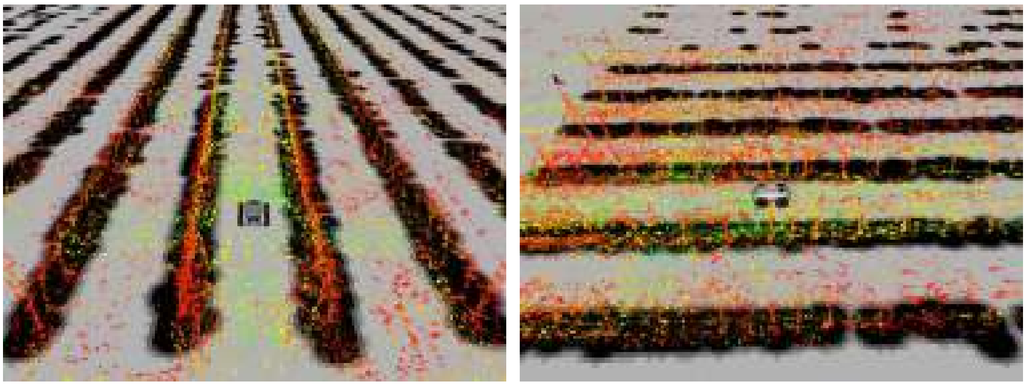

(**a**) (**b**)

Figure 2. Frontal (**a**) and lateral (**b**) view of the mobile robot, LiDAR data, and obstacles acquired in RViz from the onboard computer of the robot during the navigation in the real vineyard. The color coding reflects point height: low points (green) correspond to the ground, while higher points (orange to red) capture the vine canopy and trellis structure. The black regions in the image represent obstacles in the environment.

To follow the planned path, the robot requires a continuously updated estimate of its pose within the vineyard. Localization relies on LIO-SAM (LiDAR-Inertial Odometry via Smoothing and Mapping), a 3D SLAM framework coupling data from the LiDAR sensor and the IMU via factor graph optimization to provide an estimate of the robot position and orientation [40]. The algorithm computes orientation by integrating angular velocity measurements over short time intervals, while LiDAR data are used to refine the pose and reduce drift typically associated with dead reckoning. The navigation framework implemented also provides an Extended Kalman Filter (EKF)-based fusion stage intended to possibly integrate an absolute GNSS position and wheel odometry; however, as in this work the robot operates without GNSS, this stage is not used. Please note that the choice of LIO-SAM was driven by a quantitative comparison with other SLAM solutions performed in [41]. In that study, the navigation and mapping performance of the robotic system was evaluated in a regular and structured environment under controlled conditions, with reference to ground-truth data collected using a topographic instrument. The research reported in [41] provided methodologies and technical solutions that were integrated into the proposed system, enabling 3D mapping in vineyard environments.

During autonomous navigation, a way point is considered reached when both the position error and the heading error fall below predefined thresholds. The position error is defined as the Euclidean distance between the robot current position and the target way point, whereas the heading error corresponds to the difference between the measured and desired yaw angles. More in detail, a preliminary parametric study was carried out in simulation in which the robot has to travel through four way points placed at the vertices of a 10 × 10 m square path (with maximum desired speed equal to 0.7 m/s), sweeping five values of each parameter: position tolerance from 0.1 to 0.8 m, and angular threshold from 0.1 to 1.0 rad. The total travel time decreases as the tolerances are relaxed and reaches a plateau beyond approximately 0.4 m and 0.5 rad, while the path length remains nearly constant. Both extremes are undesirable: overly tight tolerances increase maneuvering and settling time at way points, while overly loose tolerances lead to misalignment, oscillations, and poor positioning for the next row. The selected values (0.4 m, 0.5 rad) provide a good trade-off between way point validation accuracy and navigation fluidity, and are adopted for both numerical and experimental tests.

3. Proposed Testbed

In this section, we first describe the virtual vineyard environment, which is developed to test the proposed navigation and mapping framework with extensive simulations (Section 3.1). Then, the experimental setup and the real-world vineyard scenario are illustrated in Section 3.2. Finally, Section 3.3 describes the quantitative performance metrics used to evaluate the numerical and experimental results.

3.1. Numerical Setup

In this work, we consider a Scout 2.0 skid-steered mobile robot (AgileX, Shenzhen, China). The platform is equipped with a Velodyne VLP16 LiDAR sensor (Velodyne, San Jose, CA, USA) and an Xsens MTi-630 9-axis IMU (Xsens, Enschede, The Netherlands). The simulation environment is designed in Gazebo and reproduces a realistic vineyard with 5 rows 100 m long, spaced laterally by 2.5 m. Each row consists of 10 vine segments selected from 12 different models, including variations with dense, sparse foliage, and bare wood, to maintain visual diversity. The ground is a 150 × 100 m plane. The constructed simulation environment is shown in Figure 3.

In order to provide sufficient LiDAR features for the LiDAR-based localization and mapping framework (thus mitigating the geometric degeneracy problem common in uniform corridors), the virtual environment is enriched with a diverse set of artificial and natural elements strategically distributed throughout the scene to increase geometric variability and feature distinctiveness. More in detail, the virtual environment includes structural landmarks (a shed, a cabin, a cylindrical water tank, a tractor, utility poles, and a stone wall), peripheral vegetation (five trees and eight bushes placed around the plot and at the ends of the rows), intra-plot objects (end posts of varying thicknesses for distinction, concrete markers, irrigation stakes, buckets, cans, crates, wire spools, rocks, pipes on the ground). These objects, scattered along the rows but outside the navigation path, provide distinct LiDAR features without constituting obstacles within vineyard rows, while preserving the realism of the simulated vineyard environment.

The numerical simulations aim first at defining the optimal speed for the robot in terms of the metrics illustrated in Section 3.3. In the numerical tests, six values of robot target speed are tested: 0.50, 0.60, 0.70, 0.80, 0.90, and 1.00 m/s, with 5 repeated trials per speed level (30 tests in total). Then, the repeatability performance of the proposed navigation and mapping framework is assessed using the optimal speed of the mobile platform.

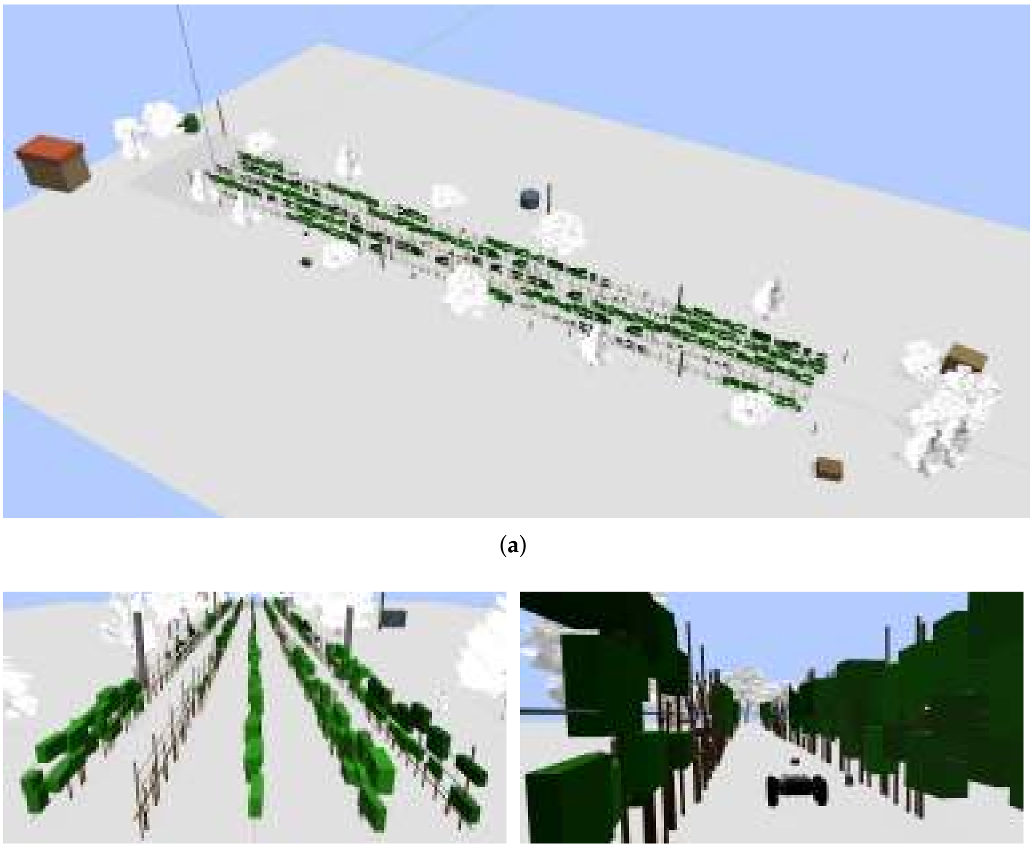

(**a**)

(**b**) (**c**)

Figure 3. Virtual vineyard developed in Gazebo for the numerical tests: aerial view (**a**); close-up view of the ends of the vine rows (**b**); internal view of a vine row, with the Scout 2.0 robot navigating between two rows (**c**).

3.2. Experimental Setup

The navigation strategy presented in this work is validated using the same model of mobile robot and onboard sensors employed in the simulations. The real robot is shown in Figure 4a. All sensor data acquisition and control processes are managed by an onboard Jetson AGX Xavier computer (NVIDIA, Santa Clara, CA, USA) running Ubuntu 18.04 and ROS Melodic. An LTE router is also integrated to provide Internet connectivity to the system.

The experimental campaign was conducted in April 2026 in a vineyard of the A. Servadei farm of the University of Udine (Northeastern Italy, Lat. 46°01′53.0″ N, Long. 13°13′29.0″ E, 113 m above sea level). The site is cultivated with Pinot gris vines with a planting density of 4000 plants per hectare, corresponding to a spacing of 1.0 m between vines and 2.5 m between rows. Five adjacent rows of the vineyard are used for the experiments, covering a total experimental area of approximately of 1325 m^2 (Figure 4b).

A set of three repeated experimental trials is conducted along the selected vineyard rows to assess the performance and repeatability of the proposed navigation framework using the same target speed of the robot, determined based on the results of the numerical tests. For each run, the robot is provided with the same sequence of way points defined in a local reference frame, corresponding to the beginning and end of each row. Based on these inputs, the system autonomously generates and follows the navigation path.

The outputs considered for evaluation include the robot position and velocity profiles over time, as well as the reconstructed 3D map of the vineyard derived from LiDAR data. The three experimental runs are carried out on the same day and under comparable environmental conditions in order to assess the repeatability of the proposed framework while limiting the influence of external factors unrelated to the navigation and mapping algorithms, such as variations in canopy conditions, soil conditions, and seasonal effects.

(**a**) (**b**)

Figure 4. Scout 2.0 mobile robot used in the experimental tests (**a**); vineyard of the A. Servadei farm of University of Udine, Italy (**b**).

3.3. Performance Metrics

The following quantitative metrics are used to evaluate the performance of the proposed navigation and mapping framework: mapping time, velocity stability, cross-track error, and point cloud reconstruction density. These metrics are detailed as follows:

- **Mapping time** represents the overall time required for the robot to complete the assigned path, namely to reach all predefined way points. This metric accounts for any stops, slowdowns, or restarts that may occur during operation, and therefore provides a comprehensive measure of navigation efficiency.
- **Velocity stability** quantifies the robot ability to maintain a consistent forward speed while traversing the rows. It is assessed by measuring the deviation of the actual linear velocity from a desired reference value, using statistical indicators such as mean, median and standard deviation. Lower variability indicates smoother motion and more reliable control performance.
- **Cross-track error (XTE)** serves as the main metric for path tracking accuracy. It is formally defined as the signed orthogonal distance between the robot center of mass and the ideal planned trajectory segment between two way points. It is strictly evaluated on the straight portions of the rows to isolate tracking performance from turning maneuvers. Since no ground-truth positioning system is available during the field experiments, the cross-track error is evaluated only in simulation, where the ground-truth pose provided by the Gazebo environment enabled the computation of the absolute path-tracking error.
- **Point cloud reconstruction density** evaluates the quality of the generated 3D map. It is defined as the number of LiDAR points per unit volume within the reconstructed environment. Higher density values correspond to more detailed representations of the vineyard, which are essential for precise monitoring and analysis tasks [41,42].

4. Results and Discussion

4.1. Numerical Results

A representative simulation run is first visually analyzed to provide a qualitative assessment of the navigation and mapping performance of the proposed framework. Figure 5 shows the reconstructed point cloud together with the robot trajectory and the predefined way points in the virtual vineyard environment. The close agreement between the planned way points and the executed trajectory, along with the uniform coverage of the reconstructed scene, highlights the capability of the system to accurately follow the desired path while generating a consistent 3D map of the environment.

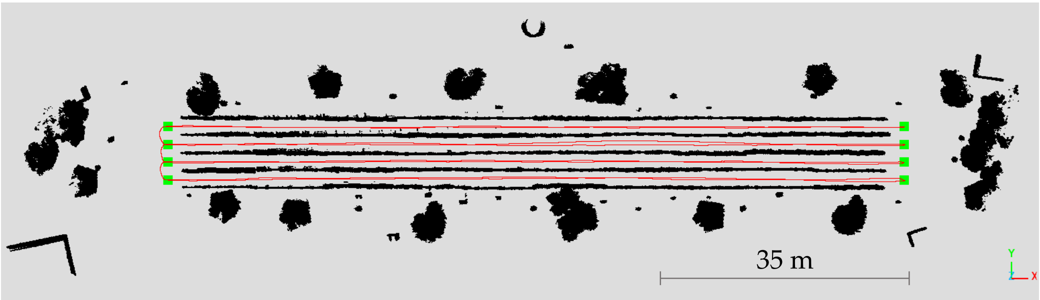

Figure 5. Example of a simulation run in the virtual vineyard: reconstructed point cloud (black), robot trajectory (red), and predefined way points (green).

Tables 1–3 provide a quantitative summary of the simulation results obtained at different target speeds.

Table 1. Simulation results: mean and standard deviation of the measured speed, median speed, mean and standard deviation of the duration, mean and standard deviation of robot stop time, as function of the target speed. The robot is considered idle when its speed is below 0.05 m/s.

v_{cmd} [m/s]	v_{mean} [m/s]	v_{med} [m/s]	Duration [s]	Stops [%]
0.50	0.47 ± 0.08	0.50	1830 ± 18	4.2 ± 0.4
0.60	0.52 ± 0.12	0.57	1580 ± 32	5.2 ± 0.8
0.70	0.63 ± 0.14	0.70	1365 ± 38	6.0 ± 0.6
0.80	0.69 ± 0.19	0.80	1241 ± 76	6.9 ± 1.2
0.90	0.76 ± 0.23	0.89	1135 ± 81	7.8 ± 2.6
1.00	0.86 ± 0.23	1.00	984 ± 12	7.5 ± 0.9

Table 2. Simulation results: number of valid tests, mean and standard deviation and RMS cross-track error, as function of the target speed.

v_{cmd} [m/s]	Valid Tests	XTE_{mean} [cm]	XTE_{RMS} [cm]
0.50	5/5	9.0 ± 1.2	11.4
0.60	5/5	9.6 ± 1.2	11.9
0.70	5/5	9.8 ± 1.0	13.3
0.80	4/5	10.1 ± 1.1	11.8
0.90	4/5	11.8 ± 2.1	15.1
1.00	4/5	11.3 ± 1.6	14.2

Table 1 reports the statistics of the measured robot speed for each commanded speed level (v_{cmd}). The median speed (v_{med}) closely matches the commanded value, confirming that the control system is able to track the desired reference during steady-state motion along the vineyard rows. However, the mean speed is systematically lower due to decelerations occurring during row transitions, turning maneuvers, and obstacle avoidance. As the target speed increases, the traversal duration decreases significantly, from approximately 1830 s at 0.50 m/s to 984 s at 1.00 m/s, highlighting the expected improvement in operational efficiency. Nevertheless, this gain is accompanied by a progressive increase in the percentage of stop time and in the standard deviation of the measured speed, indicating more frequent corrective actions and reduced motion smoothness at higher speeds. This behavior suggests a trade-off between efficiency and control stability.

Table 3. Simulation results: number of points (mean and standard deviation) of the global point cloud, number of points (mean and standard deviation) of the cropped point cloud (*), and density (mean and standard deviation) of the cropped point cloud.

v_{cmd} [m/s]	Number of Points [M]	Number of Points * [M]	Density * [pts/m^3]
0.5	5.56 ± 0.53	1.86 ± 0.25	1420 ± 56
0.6	5.19 ± 0.45	1.99 ± 0.32	1451 ± 19
0.7	5.06 ± 0.58	1.97 ± 0.33	1487 ± 40
0.8	4.77 ± 0.77	1.92 ± 0.30	1502 ± 38
0.9	4.46 ± 1.00	1.77 ± 0.44	1430 ± 45
1.0	3.85 ± 0.38	1.74 ± 0.30	1387 ± 24

Table 2 presents the localization and path-tracking performance in terms of cross-track error, computed only for valid runs, i.e., tests successfully completed without localization failure. The average XTE remains relatively low across the entire speed range, increasing from approximately 9 cm at 0.50 m/s to 11–12 cm at higher speeds. Although a slight degradation in tracking accuracy is observed as the speed increases, the variations remain limited, demonstrating that the proposed framework maintains stable path-following performance even under faster operating conditions and in geometrically repetitive vineyard environments. However, the number of failed runs increases at higher speeds, suggesting that localization robustness becomes more critical as motion dynamics intensify, likely due to reduced LiDAR scan matching reliability.

Table 3 reports the mapping performance in terms of reconstructed point cloud statistics. The point clouds acquired during the experiments are processed and analyzed in CloudCompare (v. 2.14.alpha) to evaluate the density of the resulting 3D reconstructions. Density is computed considering a local neighborhood radius of 1 m, and the point clouds are preliminary cropped to retain the five vine rows covered by the robot path, excluding peripheral points. For each speed level, the table shows the number of points in the global reconstruction, the number of points retained after cropping the vineyard area, and the corresponding point density. While the density of the cropped point cloud remains relatively stable across most speed levels, a noticeable decrease is observed at 1.0 m/s. This result indicates that, up to a certain threshold, the mapping pipeline is able to maintain a consistent level of spatial detail despite variations in robot speed. However, excessive speed reduces the sampling density of the LiDAR measurements, leading to less detailed reconstructions. This effect highlights the importance of selecting an appropriate operating speed to balance coverage efficiency and reconstruction quality.

Overall, the numerical results suggest that the speed range between 0.70 m/s and 0.80 m/s represents the best compromise between navigation efficiency, localization accuracy, and mapping quality. Within this range, the robot achieves a substantial reduction in traversal time while maintaining stable speed regulation, limited cross-track error, and high-quality 3D reconstructions. Conversely, operating above 0.80 m/s leads to increased motion variability and reduced localization robustness without significant additional benefits in terms of efficiency. Based on these considerations, a maximum speed of 0.70 m/s was selected for the experimental validation as a conservative and reliable operating condition.

To provide a more detailed insight into the system behavior at this operating point, Figure 6 reports the results of the five repeated runs with the maximum speed of 0.70 m/s. Figure 6a illustrates the robot trajectories in the x-y plane, highlighting the high repeatability of the navigation framework along the vineyard rows. The magnified views of the initial and final sections of the trajectories (Figure 6b,c) further confirm the consistency of the robot behavior during both path initialization and row transition maneuvers. Figure 6d,e report the evolution of the robot position along the x and y directions, respectively. The motion is predominantly aligned with the x-axis, corresponding to the longitudinal traversal of the vineyard rows, while variations along the y-axis occur mainly during row-switching maneuvers. Finally, Figure 6f,g show the velocity profiles, confirming that the robot maintains a nearly constant longitudinal velocity close to the commanded value, with lateral velocity components significantly different from zero only during transitions between adjacent rows.

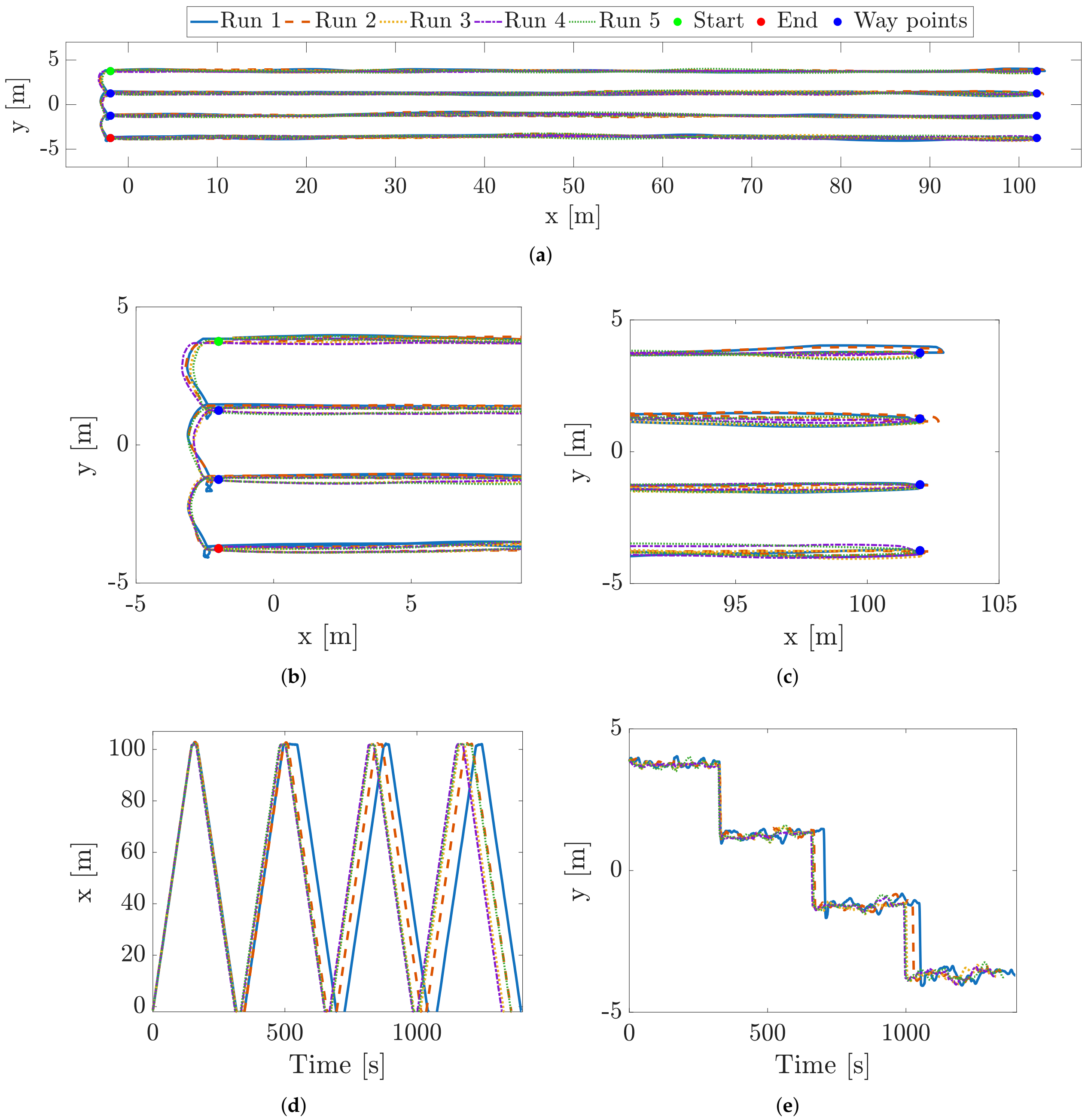

Figure 6. *Cont.*

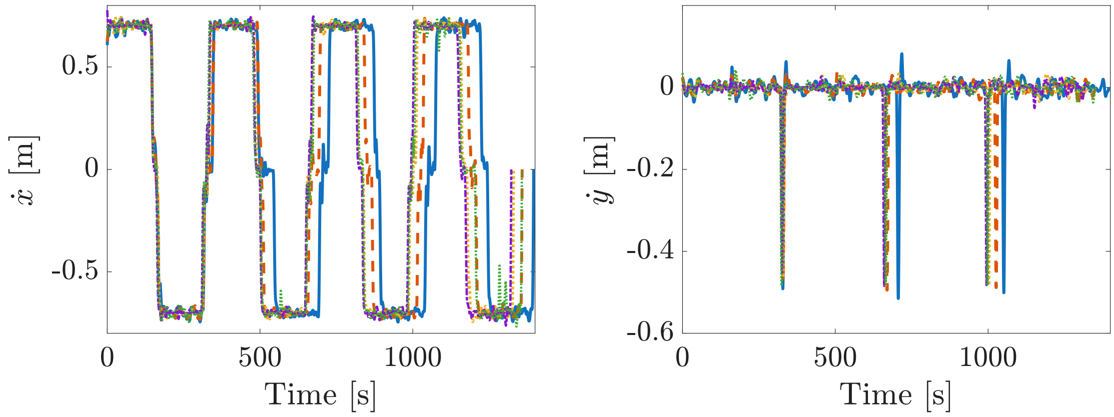

(f) (g)

Figure 6. Simulation results: robot path (**a**); magnification of the start (**b**) and end parts of the path (**c**); x position (**d**); y position (**e**); x velocity (**f**); y velocity (**g**).

4.2. Experimental Results

The experimental campaign aims to assess the repeatability and consistency of the proposed navigation framework under real-world conditions at the selected operating speed. Table 4 summarizes the main navigation metrics, including path length, mean and standard deviation of the measured speed, maximum speed, and total duration for the three runs performed in the vineyard. The results show a high level of consistency across the runs: the path length remains nearly identical (mean path length equal to 847.01 m, with maximum deviation from the mean of 0.12%), while the mean speed (mean speed equal to 0.60 m/s, with maximum deviation from the mean of 1.67%) and total duration (mean duration equal to 1415 s, with maximum deviation from the mean of 2.28%) exhibit only minor variations. This indicates that the robot is able to reliably reproduce the planned trajectories and maintain stable motion over extended distances in real operating conditions. The measured mean speed is also in close agreement with the values obtained in simulation at the same target velocity (approximately 0.60 m/s in the experiments versus about 0.63 m/s in simulation), further supporting the consistency between numerical and experimental results.

Table 4. Experimental results: path length, mean and standard deviation of the measured speed, maximum speed and total duration.

Run	Path Length [m]	v_{mean} [m/s]	v_{max} [m/s]	Duration [s]
1	846.13	0.61 ± 0.10	0.70	1383
2	846.91	0.60 ± 0.13	0.76	1419
3	848.00	0.59 ± 0.13	0.71	1444

To further analyze the robot behavior under real-world conditions, Figure 7 reports the evolution of position and velocity during the vineyard campaign. Figure 7a shows the x-y path of the robot during the three repeated runs performed at the maximum speed of 0.70 m/s. Unlike the virtual vineyard, where the row length is uniform, the real vineyard has an irregular shape: as one moves toward negative y values, the rows progressively become longer (from a minimum length of approximately 96 m to a maximum of 102 m). As a result, the length of the robot path along the x-direction varies depending on the specific row being traversed. The three runs are tightly overlaid, demonstrating high repeatability of the navigation framework within the structured vine corridors. The magnified views of the initial and final sections of the paths (Figure 7b,c) further highlight the consistency of the robot behavior during both path initialization and row transition phases.

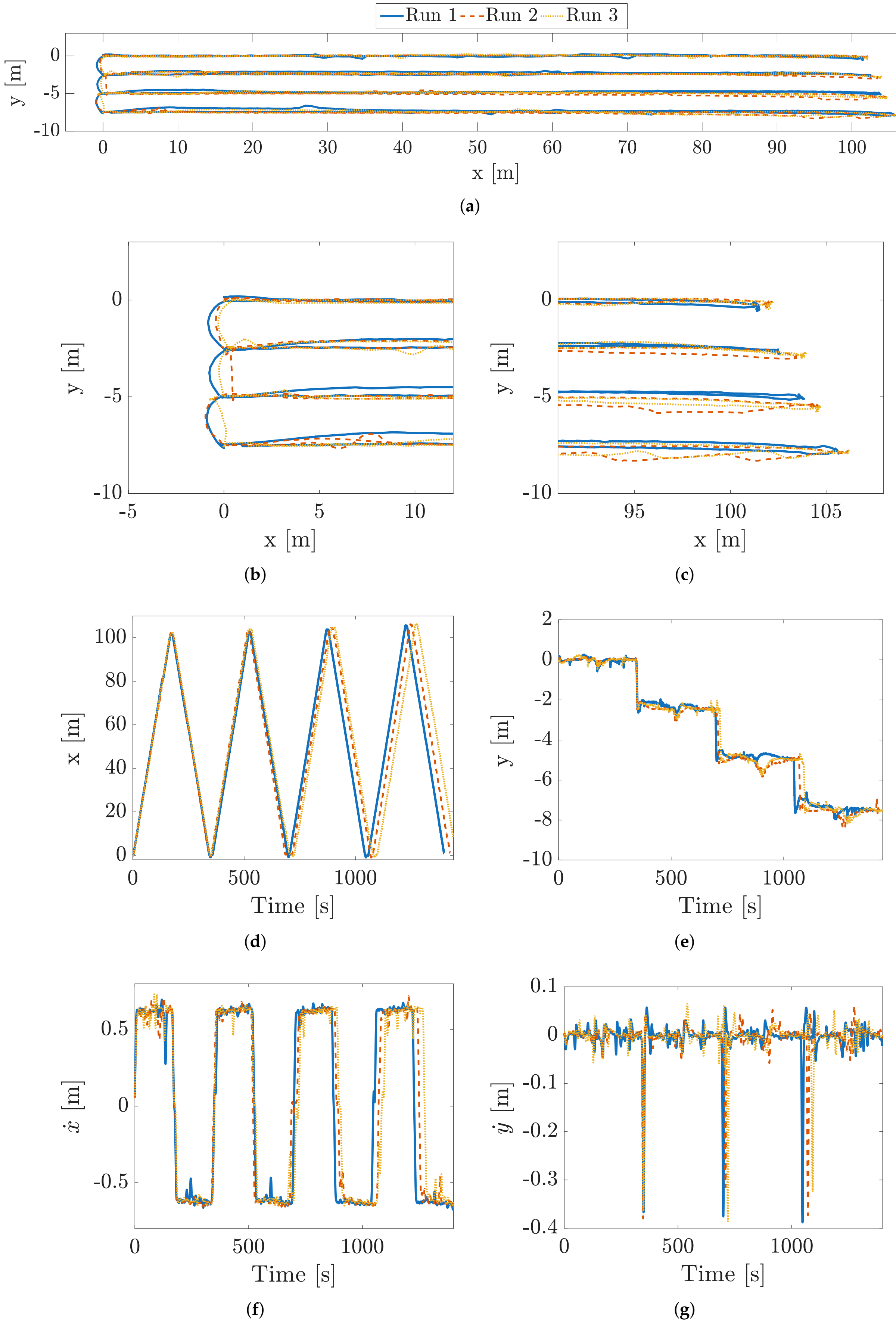

Figure 7. Experimental results: robot path (**a**); magnification of the start (**b**) and end parts of the path (**c**); x position (**d**); y position (**e**); x velocity (**f**); y velocity (**g**).

The time evolution of the robot position along the x and y directions is reported in Figure 7d,e, respectively, while the corresponding velocity profiles are shown in Figure 7f,g. To reduce measurement noise, the velocity signals are filtered using a moving average window of 40 samples. The motion is predominantly aligned with the x-axis, resulting in a nearly constant longitudinal velocity of approximately 0.6 m/s. In contrast, the lateral velocity component remains close to zero during row traversal and becomes significant only during transitions between adjacent rows.

No significant localization failures attributable to the repetitive structure of the vineyard rows are observed during the experimental campaign. Although the vineyard environment is characterized by highly repetitive geometric patterns, the presence of surrounding landmarks, including buildings, trees, poles, and other structures, provided additional geometric features that supported the LiDAR–inertial localization process.

Building on the analysis of the robot motion, the mapping performance is now evaluated in terms of point cloud reconstruction quality. A representative example of the reconstructed environment is reported in Figure 8, which shows the global point cloud obtained during a single experimental run. The resulting reconstruction captures the overall structure of the vineyard, including row geometry and canopy distribution. A more detailed comparison of the mapping performance across the three repeated runs is provided in Figure 9a–c, where the point clouds are colored according to the local density, computed in CloudCompare consistently with the methodology adopted in the numerical tests. These visualizations highlight the spatial distribution of LiDAR measurements and allow for a qualitative assessment of reconstruction uniformity.

Table 5 summarizes the quantitative results of the point cloud reconstruction for the three experimental runs, including the total number of points, the number of points within the cropped vineyard area, and the corresponding density values. The results indicate a low inter-run variability (mean density equal to 1863 pts/m^3, with maximum deviation from the mean of 6.80%), confirming the consistency of the mapping process. This observation is further supported by the density distributions shown in Figure 9, which exhibit similar shapes across the three runs. Minor differences in point cloud density can be observed at the beginning and end of the vineyard rows, likely due to slight variations in the robot approach and transition phases between adjacent rows. These local effects are consistent with the velocity profiles discussed previously and do not significantly impact the overall reconstruction quality.

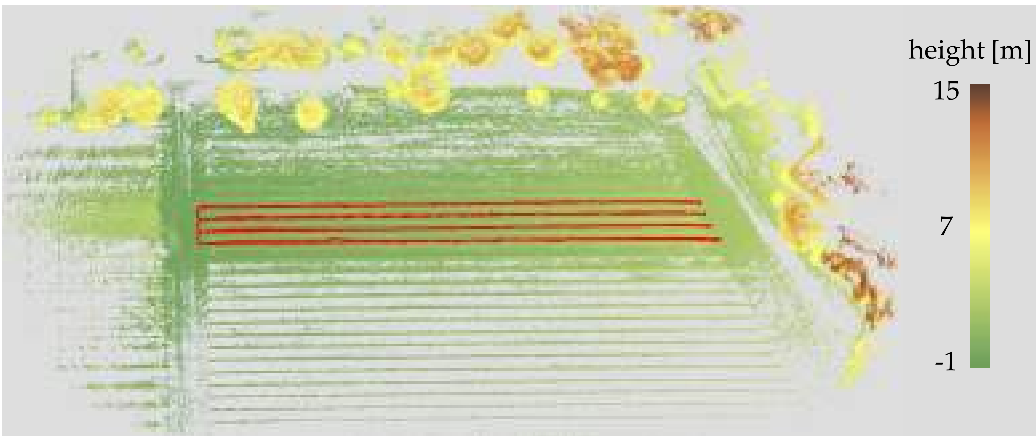

Figure 8. Global view of the 3D point cloud reconstructed during a representative experimental run. The robot trajectory (in red) is superimposed on the point cloud to illustrate the navigation path followed during the mapping process.

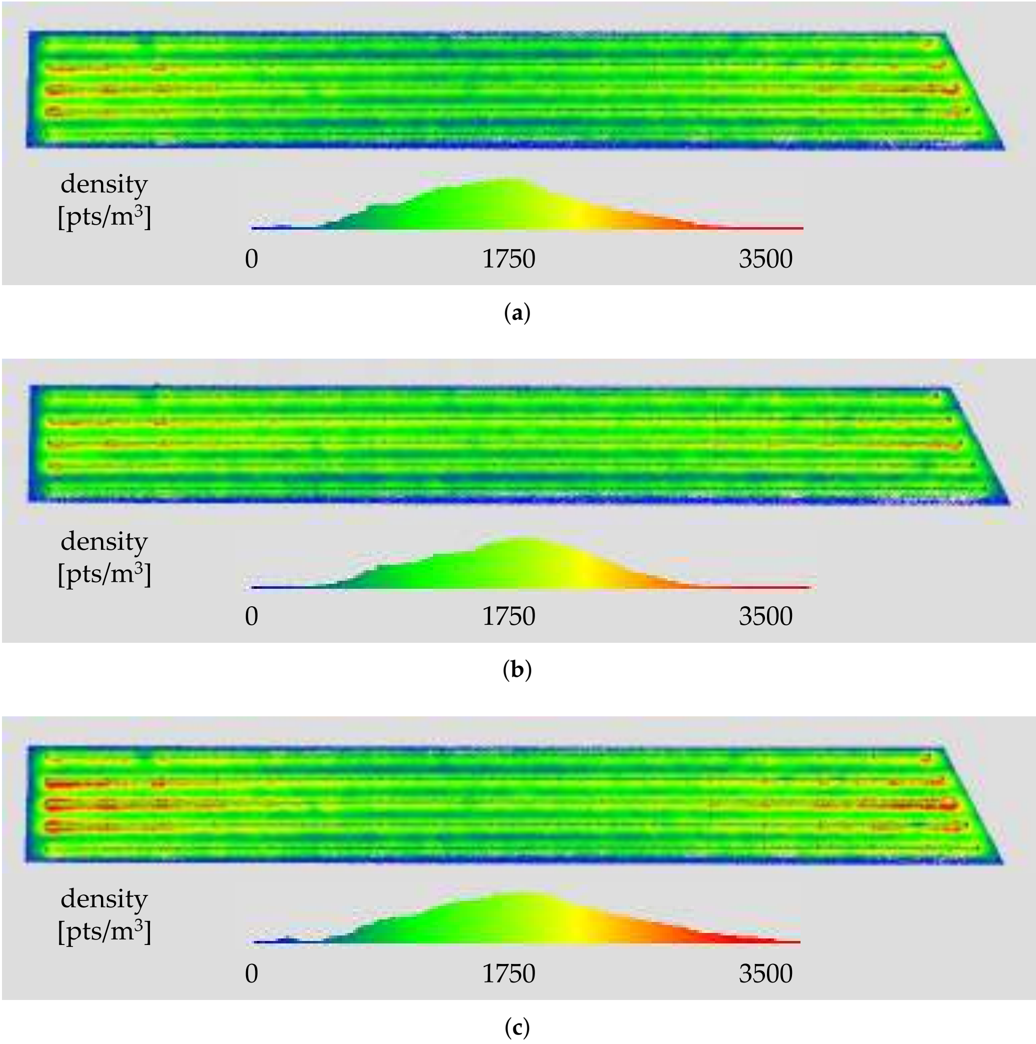

Figure 9. Point cloud density maps for the three experimental runs, computed over a local neighborhood radius of 1 m: Run 1 (**a**), Run 2 (**b**), and Run 3 (**c**). Each map is accompanied by the corresponding density histogram, providing a quantitative representation of the distribution of point density values.

Table 5. Experimental results: number of points of the global point cloud, number of points of the cropped point cloud (*), and density of the cropped point cloud.

Run	Number of Points [M]	Number of Points * [M]	Density * [pts/m^3]
1	7.389	3.392	1809
2	7.504	3.456	1791
3	8.161	3.729	1990

To further assess the repeatability of the mapping framework, a Cloud-to-Cloud (C2C) distance analysis is performed in CloudCompare by comparing the cropped point clouds obtained from the repeated experimental runs. The point cloud acquired during Run 1 is used as the reference model, while the reconstructions from Runs 2 and 3 are compared against it. Prior to the C2C computation, the point clouds are co-registered using the Iterative Closest Point algorithm to compensate for residual global misalignments potentially arising from differences in the initialization of the local reference frame. The analysis yields a mean C2C distance of 0.028 m ($\pm$0.022 m) between Run 1 and Run 2, and 0.024 m ($\pm$0.019 m) between Run 1 and Run 3. These low deviations indicate a high degree of consistency among the reconstructed vineyard maps, confirming that the proposed navigation and mapping framework is capable of generating repeatable 3D reconstructions across independent experimental runs under real operating conditions.

During the experimental campaign, the variability among runs arises from several factors that are inherently present in outdoor agricultural environments, including variations in terrain traversability, local wheel-soil interactions, vegetation motion caused by wind, and changes in the LiDAR observations used for localization and obstacle avoidance. These factors can slightly affect both the robot trajectory and the generated point clouds, leading to small differences among repeated runs.

Overall, although absolute positioning accuracy could not be quantified in the field, the experimental tests demonstrate a good degree of repeatability in terms of trajectory execution, velocity profiles, path length, and 3D reconstruction across repeated runs. While the limited number of repetitions does not allow a rigorous statistical significance analysis, the low dispersion observed across the three independent trials provide indirect evidence of the robustness and consistency of the proposed framework during long-distance autonomous operations in a real vineyard. The robot successfully completed autonomous runs exceeding 800 m without relying on GNSS corrections, maintaining consistent trajectories and point cloud reconstructions across different runs. Furthermore, the experimental results are in agreement with the trends observed in simulation, supporting the validity of the simulation environment as a reliable tool for performance assessment and parameter tuning.

5. Conclusions

In this paper, the numerical and experimental validation of a LiDAR–inertial navigation and mapping framework for mobile robots operating in vineyard-like environments was presented. A realistic simulated vineyard environment, reproducing the geometric structure of vine rows, was first developed to assess the performance of the proposed approach using multiple metrics, including mapping time, velocity stability, path tracking error, and point cloud reconstruction density. The framework was then validated in a real vineyard using a Scout 2.0 mobile robot that performed extensive tests up to 800 m long. Numerical and experimental results demonstrated the feasibility of the proposed navigation and mapping strategy, as well as its robustness over extensive repeated trials.

Moreover, a strong agreement between numerical and experimental results was observed, confirming that the trends identified in simulation are consistent with real-world behavior. This validates the use of the proposed simulation environment as an effective tool for preliminary testing and parameter tuning, enabling the identification of suitable operating conditions prior to field deployment. Such a simulation-driven approach can reduce the need for extensive experiments, lowering time, cost, and operational risks.

Future work will include the integration of a RTK-GNSS system to obtain an independent ground-truth reference and enable a quantitative evaluation of the absolute localization accuracy in real operating conditions during surveying in the vineyard. In addition, a reference point cloud acquired through geomatics surveying techniques will be considered to provide an objective benchmark for the quantitative validation of the 3D mapping accuracy. Furthermore, we will focus on the development of an AI-based navigation pipeline to improve the path planning and obstacle avoidance of the robot based on online visual information.

Author Contributions: Conceptualization, methodology, formal analysis, investigation, validation, L.S. and E.M.; software, data curation, A.A.; writing—original draft preparation, A.A., L.S. and E.M.; writing—review and editing, L.S. and E.M.; visualization, A.A., L.S. and E.M.; resources, supervision, project administration, funding acquisition, L.S., E.M. and A.G. All authors have read and agreed to the published version of the manuscript.

Funding: This research was developed within the Laboratory for Big Data, IoT, Cyber Security (LABIC) funded by Friuli Venezia Giulia region (Italy), and the Laboratory for Artificial Intelligence for Human-Robot Collaboration (AI4HRC) funded by Fondazione Friuli (Italy). This study was carried out within the Agritech National Research Center, and received funding from the European Union Next-Generation EU (National Recovery and Resilience Plan, PNRR, Mission 4, Component 2, Investiment 1.4—D.D. 1032 17/06/2022, CN00000022). Eleonora Maset acknowledges financial support from the "Programma Operativo Complementare (POC) 2014–2020 of the Friuli Venezia Giulia Autonomous Region—Support for advanced training within the regional university system—Extraordinary measure for the extension or renewal of research grants and fixed-term type A researcher contracts", Decree no. 41355/GRFVG of 7 August 2025—CUP G23C25000880002—Operation code 2025/13846—Project code 2025/13846/11. This manuscript reflects only the authors' views and opinions, neither the European Union nor the European Commission can be considered responsible for them.

Data Availability Statement: Data related to the real-world experiments are available at the following link: https://doi.org/10.5281/zenodo.20590576.

Acknowledgments: The authors would like to thank Paolo Sivilotti, Moreno Greatti and Gianni Tassan for allowing us to perform experiments in the vineyard of Azienda Agraria A. Servadei of the University of Udine (Italy). We also thank Jules Desaintjan for his assistance during the experimental tests.

Conflicts of Interest: The authors declare no conflicts of interest.

Abbreviations

The following abbreviations are used in this manuscript:

C2C	Cloud-to-Cloud
DOF	Degree of freedom
EKF	Extended Kalman Filter
GNSS	Global Navigation Satellite Systems
IMU	Inertial Measurement Unit
LiDAR	Light Detection and Ranging
LIO-SAM	LiDAR-Inertial Odometry via Smoothing and Mapping
ROS	Robot Operating System
RMS	Root Mean Square
RTK	Real-Time Kinematics
SLAM	Simultaneous Localization and Mapping
SDG	Sustainable Development Goal
TEB	Timed Elastic Band
XTE	Cross-track error
VO	Visual Odometry

References

1. Tardaguila, J.; Stoll, M.; Gutiérrez, S.; Proffitt, T.; Diago, M.P. Smart applications and digital technologies in viticulture: A review. *Smart Agric. Technol.* **2021**, *1*, 100005. [CrossRef]
2. United Nations. *Sustainable Development Goals*; United Nations: New York, NY, USA, 2015.
3. Willekens, A.; Temmerman, S.; Wyffels, F.; Pieters, J.G.; Cool, S.R. Development of an agricultural robot taskmap operation framework. *J. Field Robot.* **2025**, *42*, 4256–4287. [CrossRef]
4. Morbidini, F.; Samanta, A.; Maucieri, C.; Karydis, K.; Mauk, P.A.; Skaggs, T.H.; Scudiero, E. Robotic mapping of soil volumetric water content with geospatial soil apparent electrical conductivity in micro-irrigated citrus orchards in California. *Comput. Electron. Agric.* **2026**, *245*, 111540. [CrossRef]
5. Tiozzo Fasiolo, D.; Scalera, L.; Maset, E.; Gasparetto, A. Recent trends in mobile robotics for 3D mapping in agriculture. In *Advances in Service and Industrial Robotics. RAAD 2022*; Müller, A., Brandstötter, M., Eds.; Mechanisms and Machine Science; Springer: Cham, Switzerland, 2022; Volume 120, pp. 428–435.

6. Tiozzo Fasiolo, D.; Pichierri, A.; Sivilotti, P.; Scalera, L. An analysis of the effects of water regime on grapevine canopy status using a UAV and a mobile robot. *Smart Agric. Technol.* **2023**, *6*, 100344. [CrossRef]
7. Chatziparaschis, D.; Scudiero, E.; Sams, B.; Karydis, K. An Annotation-to-Detection Framework for Autonomous and Robust Vine Trunk Localization in the Field by Mobile Agricultural Robots. *arXiv* **2026**, arXiv:2603.26724.
8. Yang, R.; Zhang, X.; Chen, Y.; Huang, X.; Feng, S. A Real-Time Semantic 3D Vineyard Mapping and Fruit Localization System for Yield Estimation in Dynamic Vineyards. *Smart Agric. Technol.* **2026**, *13*, 101784. [CrossRef]
9. Gao, X.; Li, J.; Fan, L.; Zhou, Q.; Yin, K.; Wang, J.; Song, C.; Huang, L.; Wang, Z. Review of wheeled mobile robots' navigation problems and application prospects in agriculture. *IEEE Access* **2018**, *6*, 49248–49268. [CrossRef]
10. Mammarella, M.; Comba, L.; Biglia, A.; Dabbene, F.; Gay, P. Cooperation of unmanned systems for agricultural applications: A case study in a vineyard. *Biosyst. Eng.* **2022**, *223*, 81–102. [CrossRef]
11. Zhang, J.; Su, L.; Bai, Z.; Yang, S.X.; Li, P.; Hong, S.; Ma, W.; Song, L. Research on Path Planning and Trajectory Tracking for Inspection Robots in Orchard Environments. *Agriculture* **2026**, *16*, 415. [CrossRef]
12. Liang, Z.; Wang, L.; Wang, H.; Zhang, B.; Liu, C. Autonomous obstacle avoidance and path planning for mobile robots in orchard environments combining with map construction and positioning methods. *Comput. Electron. Agric.* **2026**, *244*, 111514. [CrossRef]
13. de Silva, R.; Cox, J.; Heselden, J.R.; Popović, M.; Cadena, C.; Polvara, R. Semantic Landmark Particle Filter for Robot Localisation in Vineyards. *arXiv* **2026**, arXiv:2603.10847.
14. B Guerrero, H.; Montenegro, D.C.; Jutinico, A.L. Reactive fuzzy control and field validation of a low-cost autonomous tracked robot for plantain crop row following. *Eng. Res. Express* **2026**, *8*, 045227. [CrossRef]
15. Usu, K.; Yamasaki, Y.; Ishii, K.; Noguchi, N. Global self-localization and navigation using 3D-LiDAR for headland turning in vineyards. *Smart Agric. Technol.* **2025**, *12*, 101296. [CrossRef]
16. Pappalettera, A.; Mantriota, G.; Reina, G. Safety-aware headland turning in sloping vineyards for field robots. *Mech. Based Des. Struct. Mach.* **2026**, *54*, 2652526. [CrossRef]
17. Santos, L.; Santos, F.; Mendes, J.; Costa, P.; Lima, J.; Reis, R.; Shinde, P. Path planning aware of robot's center of mass for steep slope vineyards. *Robotica* **2020**, *38*, 684–698.
18. Schönegg, T.; Tuna, T.; Yang, F.; Waibel, G.; Mattamala, M.; Hutter, M. Global path planning for autonomous vehicles in orchards and vineyards. In *Proceedings of the 13th International Workshop on Robot Motion and Control*; IEEE: Piscataway, NJ, USA, 2024; pp. 1–8.
19. Cerrato, S.; Aghi, D.; Mazzia, V.; Salvetti, F.; Chiaberge, M. An adaptive row crops path generator with deep learning synergy. In *Proceedings of the 6th Asia-Pacific Conference on Intelligent Robot Systems (ACIRS)*; IEEE: Piscataway, NJ, USA, 2021; pp. 6–12.
20. Shen, Y.; Shen, Y.; Zhang, Y.; Huo, C.; Shen, Z.; Su, W.; Liu, H. Research Progress on Path Planning and Tracking Control Methods for Orchard Mobile Robots in Complex Scenarios. *Agriculture* **2025**, *15*, 1917. [CrossRef]
21. Chakraborty, M.; Khot, L.R.; Sankaran, S.; Jacoby, P.W. Evaluation of mobile 3D light detection and ranging based canopy mapping system for tree fruit crops. *Comp. Electr. Agric.* **2019**, *158*, 284–293. [CrossRef]
22. Silwal, A.; Yandun, F.; Nellithimaru, A.K.; Bates, T.; Kantor, G. Bumblebee: A path towards fully autonomous robotic vine pruning. *Field Rob.* **2022**, *2*, 1661–1696. [CrossRef]
23. Betrò, G.; Pascuzzi, S.; Paciolla, F. A GNSS-free LiDAR-based navigation architecture for autonomous inter-row operation under sparse or absent vegetation conditions. *Smart Agric. Technol.* **2026**, *14*, 102106. [CrossRef]
24. Zaman, S.; Comba, L.; Biglia, A.; Aimonino, D.R.; Barge, P.; Gay, P. Cost-effective Visual Odometry system for vehicle motion control in agricultural environments. *Comput. Electron. Agric.* **2019**, *162*, 82–94. [CrossRef]
25. Hroob, I.; Polvara, R.; Molina, S.; Cielniak, G.; Hanheide, M. Benchmark of visual and 3D LiDAR SLAM systems in simulation environment for vineyards. In *Proceedings of the Annual Conference Towards Autonomous Robotic Systems*; Springer: Cham, Switzerland, 2021; pp. 168–177.
26. Gao, P.; Jiang, J.; Song, J.; Xie, F.; Bai, Y.; Fu, Y.; Wang, Z.; Zheng, X.; Xie, S.; Li, B. Canopy volume measurement of fruit trees using robotic platform loaded LiDAR data. *IEEE Access* **2021**, *9*, 156246–156259. [CrossRef]
27. Teng, H.; Wang, Y.; Chatziparaschis, D.; Karydis, K. Adaptive LiDAR odometry and mapping for autonomous agricultural mobile robots in unmanned farms. *Comput. Electron. Agric.* **2025**, *232*, 110023. [CrossRef]
28. Aghi, D.; Cerrato, S.; Mazzia, V.; Chiaberge, M. Deep semantic segmentation at the edge for autonomous navigation in vineyard rows. In *Proceedings of the 2021 IEEE/RSJ International Conference on Intelligent Robots and Systems (IROS)*; IEEE: Piscataway, NJ, USA, 2021; pp. 3421–3428.
29. Choi, S.; Han, X.; Chang, E.; Jeong, H. LiDAR-IMU Sensor Fusion-Based SLAM for Enhanced Autonomous Navigation in Orchards. *Agriculture* **2025**, *15*, 1899. [CrossRef]
30. Fujinaga, T. Autonomous navigation method for agricultural robots in high-bed cultivation environments. *Comput. Electron. Agric.* **2025**, *231*, 110001. [CrossRef]
31. Crocetti, F.; Bellocchio, E.; Dionigi, A.; Felicioni, S.; Costante, G.; Fravolini, M.L.; Valigi, P. ARD-VO: Agricultural robot data set of vineyards and olive groves. *J. Field Robot.* **2023**, *40*, 1678–1696. [CrossRef]

32. Polvara, R.; Molina, S.; Hroob, I.; Papadimitriou, A.; Tsiolis, K.; Giakoumis, D.; Likothanassis, S.; Tzovaras, D.; Cielniak, G.; Hanheide, M. Bacchus Long-Term (BLT) data set: Acquisition of the agricultural multimodal BLT data set with automated robot deployment. *J. Field Robot.* **2024**, *41*, 2280–2298.
33. Cañadas-Aránega, F.; Blanco-Claraco, J.L.; Moreno, J.C.; Rodriguez-Diaz, F. Multimodal mobile robotic dataset for a typical mediterranean greenhouse: The greenbot dataset. *Sensors* **2024**, *24*, 1874. [CrossRef] [PubMed]
34. Slaviček, P.; Hrabar, I.; Kovačić, Z. Generating a Dataset for Semantic Segmentation of Vine Trunks in Vineyards Using Semi-Supervised Learning and Object Detection. *Robotics* **2024**, *13*, 20. [CrossRef]
35. Tiozzo Fasiolo, D.; Scalera, L.; Maset, E.; Gasparetto, A. The FriûlBot dataset: Experimental validation of an autonomous ground robot for vineyard 3D mapping. *Robot. Auton. Syst.* **2025**, *197*, 105283. [CrossRef]
36. Jang, S.H.; Cho, H.R.; Hong, H.G.; Kwon, T.H.; Cho, Y.J.; Yun, H.Y.; Lee, Y.J.; Ahn, W.J.; Lim, M.T. FruitTrackDB: A multi-sensor dataset for intelligent navigation in real orchard environments. *Intell. Serv. Robot.* **2026**, *19*, 50. [CrossRef]
37. Tiozzo Fasiolo, D.; Scalera, L.; Maset, E.; Lesquerré-Caudebez, B.; Fusiello, A.; Beinat, A.; Gasparetto, A. A Navigation Approach for Autonomous Mobile Robots in Sustainable Agriculture. In *Proceedings of I4SDG Workshop 2025—IFToMM for Sustainable Development Goals. I4SDG 2025*; Carbone, G., Quaglia, G., Eds.; Mechanisms and Machine Science; Springer: Cham, Switzerland, 2025; Volume 179, pp. 399–408.
38. Eitan, M.E.; Sachin, C. carrot_planner. 2018. Available online: http://wiki.ros.org/carrot_planner?distro=melodic (accessed on 15 May 2026).
39. Rösmann, C.; Hoffmann, F.; Bertram, T. Integrated online trajectory planning and optimization in distinctive topologies. *Robot. Auton. Syst.* **2017**, *88*, 142–153. [CrossRef]
40. Shan, T.; Englot, B.; Meyers, D.; Wang, W.; Ratti, C.; Rus, D. LIO-SAM: Tightly-coupled LiDAR inertial odometry via smoothing and mapping. In *Proceedings of the International Conference on Intelligent Robots and Systems (IROS)*; IEEE: Piscataway, NJ, USA, 2020; pp. 5135–5142.
41. Tiozzo Fasiolo, D.; Scalera, L.; Maset, E. Comparing LiDAR and IMU-based SLAM approaches for 3D robotic mapping. *Robotica* **2023**, *41*, 2588–2604. [CrossRef]
42. Maset, E.; Scalera, L.; Beinat, A.; Visintini, D.; Gasparetto, A. Performance investigation and repeatability assessment of a mobile robotic system for 3D mapping. *Robotics* **2022**, *11*, 54. [CrossRef]